

# La<sub>2</sub>SrCr<sub>2</sub>O<sub>7</sub>: Controlling the tilting distortions of $n = 2$ Ruddlesden-Popper phases through A-site cation order.

Ronghuan Zhang<sup>a</sup>, Brian M. Abbett<sup>b</sup>, Gareth Read<sup>a</sup>, Franz Lang<sup>c</sup>, Tom Lancaster<sup>d</sup>, T. Thao Tran<sup>e</sup>, P. Shiv Halasyamani<sup>e</sup>, Stephen J. Blundell<sup>c</sup>, Nicole A. Benedek<sup>f\*</sup>, and Michael A. Hayward<sup>a\*</sup>

<sup>a</sup> Department of Chemistry, University of Oxford, Inorganic Chemistry Laboratory, South Parks Road, Oxford, OX1 3QR, UK.

<sup>b</sup> School of Applied and Engineering Physics, Cornell University, Ithaca, New York 14853, USA

<sup>c</sup> Department of Physics, Clarendon Laboratory, University of Oxford, Parks Road, Oxford, OX1 3PU, UK.

<sup>d</sup> Department of Physics, Durham University, South Road, Durham DH1 3LE, UK

<sup>e</sup> Department of Chemistry, University of Houston, 112 Fleming Building, Houston, Texas 77204-5003, USA

<sup>f</sup> Department of Materials Science and Engineering, Cornell University, Ithaca, New York 14853, USA

*Supporting Information Placeholder*

**ABSTRACT:** Structural characterization by neutron diffraction, supported by magnetic, SHG and  $\mu^+$ SR data, reveals that the  $n = 2$  Ruddlesden-Popper phase La<sub>2</sub>SrCr<sub>2</sub>O<sub>7</sub> adopts a highly unusual structural configuration in which the cooperative rotations of the CrO<sub>6</sub> octahedra are out of phase in all three Cartesian directions ( $\Phi\Phi\Phi_z / \Phi\Phi\Phi_z; a^+a^-c^- / a^+a^-c^-$ ) as described in space group  $A2/a$ . First principles DFT calculations indicate that this unusual structural arrangement can be attributed to coupling between the La/Sr A-site distribution and the rotations of the CrO<sub>6</sub> units, which combine to relieve the local deformations of the chromium-oxygen octahedra. This coupling suggests new chemical ‘handles’ by which the rotational distortions or A-site cation order of Ruddlesden-Popper phases can be directed to optimize physical behavior. Low-temperature neutron diffraction data and  $\mu^+$ SR data indicate La<sub>2</sub>SrCr<sub>2</sub>O<sub>7</sub> adopts a G-type antiferromagnetically ordered state below  $T_N \sim 260$ K.

## Introduction

The ABO<sub>3</sub> perovskite structure is adopted by complex metal oxide phases with a very wide variety of chemical compositions. Indeed it is possible to incorporate all the transition metals within perovskite frameworks, many of them in a number of different oxidation states. The ubiquity and chemical diversity of perovskite oxide phases primarily arises from the intrinsic thermodynamic stability imparted by the close packed nature of the structure (the framework can be thought of as being derived from a cubic close packed lattice). However, unlike many other structure types derived from close-packed arrangements, the perovskite structure can form thermodynamically stable phases incorporating combinations of A- and B-cations with a large range of radius ratios, due to the mechanical flexibility imparted into perovskite frameworks by the facile collective rotations of the constituent, apex-linked, BO<sub>6</sub> octahedra.

In addition to imbuing the perovskite framework with mechanical flexibility, the tilting and twisting distortions of perovskite oxide phases can have a large influence on their physical properties. This can be seen most directly by observing that these facile collective distortions typically lead to changes (tightening) of the B-O-B bond angles between linked BO<sub>6</sub> octahedra, while leaving the internal coordinates of the BO<sub>6</sub> units largely unchanged. As a result the distor-

tions of transition metal perovskite oxides predictably modify the alignment of, and thus the interactions between, the d-orbitals on adjacent transition metal centers. Thus by adjusting the B-O-B bond angles of a phase by modifying the A:B cation radius ratio (conveniently parameterized as the Goldschmidt tolerance factor,  $t = \langle A-O \rangle / \sqrt{2} \times \langle B-O \rangle$ )<sup>1</sup> the electronic band width of a system can be tuned to drive a change from metallic to semiconducting behavior, as observed for the LnNiO<sub>3</sub> (Ln = lanthanide) series.<sup>2</sup> Similarly, the B-O-B bond angle can also be used to tune the strength of superexchange interactions in insulating phases, as observed for the LnFeO<sub>3</sub> series.<sup>3</sup>

Over and above modifications to the electronic and magnetic coupling between B-cations, the cooperative structural distortions of perovskite phases can have a more dramatic influence on the physical behavior of materials, because they lower the crystallographic symmetry of the perovskite framework, allowing phases to exhibit behavior forbidden on symmetry grounds in materials with the cubic lattice symmetry of the undistorted, aristotype perovskite structure. Many of the most desirable symmetry-dependent physical behaviors, such as ferroelectricity, piezoelectricity and second-harmonic generation (SHG), require a lifting of inversion symmetry. Unfortunately, the reciprocal nature of the collective rotations of the apex-linked BO<sub>6</sub> units in perovskite frameworks means that in a material in which the BO<sub>6</sub> units are continuously linked in all three dimensions, inversion symmetry can only be broken by these rotations if they are combined with A-site or B-site cation order.<sup>4-7</sup>

The requirement to control both the cation order and the collective tilting and twisting distortions of perovskite phases significantly increases the synthetic difficulty of preparing non-centrosymmetric (NCS) materials. Fortunately, some relief can be found in the recent theoretical and experimental observations that inversion symmetry can be broken in the layered variants of the perovskite structure by the collective rotations of the constituent BO<sub>6</sub> octahedra alone, without the need for cation order.<sup>8</sup> Thus, for example, if the appropriate collective tilting and twisting arrangement of the BO<sub>6</sub> octahedra is induced into an A<sub>3</sub>B<sub>2</sub>O<sub>7</sub>,  $n = 2$  Ruddlesden-Popper phase,<sup>9,10</sup> or an A'AB<sub>2</sub>O<sub>7</sub>,  $n = 2$  Dion-Jacobson phase<sup>11-15</sup> the inversion symmetry of the aristotype structures can be broken to yield NCS materials.

It is clear from the examples above that the collective rotations of the octahedra in phases with 3D perovskite, or related 2D Ruddlesden-Popper or Dion-Jacobson structures, can have a decisive influ-

ence on the physical properties of materials with these structure types. This provides a strong motivation to develop a better understanding of the factors that influence which of the many possible ordered tilting and twisting schemes is adopted by a particular phase, so that we can better direct these structural distortions to tune materials to exhibit desired behavior.

In this paper we describe the detailed structural characterization and analysis of the  $n = 2$  Ruddlesden-Popper oxide  $\text{La}_2\text{SrCr}_2\text{O}_7$ . Initially this phase was prepared to act as a substrate for a topochemical fluorination study focused on synthesizing phases containing  $\text{Cr}^{4+}$ .<sup>16</sup> However detailed analysis of the structure of  $\text{La}_2\text{SrCr}_2\text{O}_7$  revealed a novel interaction which couples the A-site La/Sr cation distribution to the ordered twisting distortions of the  $\text{CrO}_6$  octahedra, offering the opportunity to tune one of these structural features by modifying the other.

### Experimental

**Synthesis.** Samples of  $\text{La}_2\text{SrCr}_2\text{O}_7$  were prepared by grinding together suitable quantities of  $\text{La}_2\text{O}_3$  (99.999%, dried at 900 °C),  $\text{SrCO}_3$  (99.99%),  $\text{Cr}_2\text{O}_3$  (99.97%) and then heating the mixtures in air at 1000 °C for 20 h to decompose the carbonate. The resulting material was then pressed into 13 mm diameter pellets and heated at 1460 °C for 4 periods of 55 h under flowing argon.

**Characterisation.** X-ray powder diffraction data were collected using a PANalytical X'pert diffractometer incorporating an X'celerator position-sensitive detector (monochromatic  $\text{Cu K}\alpha 1$  radiation). Neutron powder diffraction data were collected using the GEM diffractometer (ISIS neutron source, U.K) from samples contained in cylindrical vanadium cans. Rietveld profile refinements were performed using the GSAS suite of programs.<sup>17</sup> Magnetization data were collected from powder samples using a Quantum Design MPMS SQUID magnetometer in an applied field of 100 Oe. The  $\mu^+\text{SR}$  experiments were carried out at the Swiss Muon Source, PSI, Switzerland. In a  $\mu^+\text{SR}$  experiment, spin-polarized muons were implanted in the bulk of a material and the time-dependence of their polarization monitored by recording the angular distribution of the subsequent positron decay. Powder SHG measurements were performed using a modified Kurtz-NLO system<sup>18,19</sup> incorporating a pulsed Nd:YAG laser with a wavelength of 1064 nm. The equipment and methodology has been described in detail previously.<sup>20</sup>

**DFT calculations.** First principles calculations were carried out using the *Vienna Ab initio Simulation Package*.<sup>21,22</sup> The PBEsol exchange-correlation potential and projector augmented wave pseudopotentials<sup>23,24</sup> were used throughout. The valence electron configurations for each pseudopotential were:  $5s^2 5p^6 5d^1 6s^2$  for La;  $4s^2 4p^6 5s^2$  for Sr;  $3s^2 3p^6 3d^5 4s^1$  for Cr; and  $2s^2 2p^4$  for O. The calculations were spin-polarized and included a Hubbard  $U$  of 4.0 eV for the Cr 3d electrons (changing  $U$  to 2.0 or 6.0 eV did not qualitatively change the results of our structural analysis of the  $A2/a$  structure). A complete study on the effects of including a Hubbard  $U$  on the La 4f electrons was not performed, but our results indicate that this would mainly reduce the amplitude of octahedral rotations in our relaxed structures, which does not alter our conclusions. Relaxations were considered converged when the force on each atom became smaller than 1 meV/Å. A plane wave cutoff of 600 eV was used throughout, a  $6 \times 6 \times 1$  Monkhorst-Pack mesh was used for the 24-atom simulation cells and a  $4 \times 4 \times 1$  Monkhorst-Pack mesh was used for all other simulation cells. This energy cutoff and  $k$ -point mesh resulted in an energy difference between relaxed  $A_{mm}$  and  $I4/mmm$  structures that is converged to within 0.05 meV per formula unit, compared to higher plane wave cutoffs and denser  $k$ -point meshes.

### Results

**Structural refinement of  $\text{La}_2\text{SrCr}_2\text{O}_7$ .** X-ray and neutron powder diffraction data collected from  $\text{La}_2\text{SrCr}_2\text{O}_7$  could be readily indexed using an orthorhombic unit cell ( $a = 5.492$  Å,  $b = 5.479$  Å,  $c = 20.182$  Å) consistent with a distorted  $n = 2$  Ruddlesden-Popper type structure. The extinction conditions of the diffraction data indicate an A-

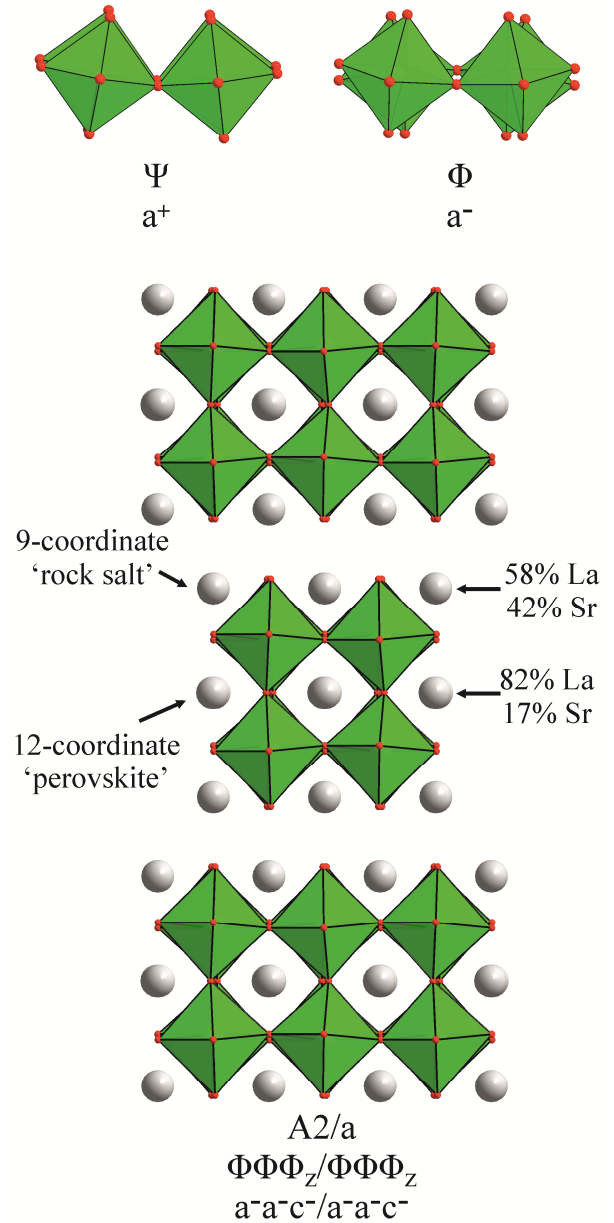


**Figure 1.** (Top) The in-phase ( $\Psi$ ,  $a^+$ ) and out of phase ( $\Phi$ ,  $a^-$ ) rotations of apex-linked octahedra. (Bottom) A representation of the refined structure of  $\text{La}_2\text{SrCr}_2\text{O}_7$  viewed along the (1,1,0) direction. Grey, green and red spheres represent La/Sr, Cr and O respectively.

centering of the unit cell, with the stated setting of the lattice parameters.

Aleksandrov and Bartolome performed a symmetry analysis of the possible cooperative twisting distortions of the  $\text{BO}_6$  octahedra in  $\text{A}_3\text{B}_2\text{O}_7$   $n = 2$  Ruddlesden-Popper phases.<sup>25</sup> They used a notation to describe the cooperative twisting of the  $\text{BO}_6$  octahedra in which  $\Psi$  describes a distortion in which neighboring octahedra are rotated in the same direction (in-phase) and  $\Phi$  describes a the rotation of neighboring octahedra in opposing directions (out of phase), as shown in Figure 1. In addition it is observed that the rotations of octahedra around the  $z$ -axis are distinct from those around  $x$ - or  $y$ -axes.

The A-centered orthorhombic extinction conditions observed in the diffraction data collected from  $\text{La}_2\text{SrCr}_2\text{O}_7$  are compatible with the symmetry of 6 of the cooperative distortions described by Aleksandrov and Bartolome, as listed in Table 1. Thus crystallographic

Space Group	Tilt System	Glazer Tilt	$\chi^2$	wRp (%)	Rp (%)
Acam	00 $\Psi_z$ /00 $\Psi_z$	$a^0a^0c^+/a^0a^0c^+$	7.20	5.16	4.10
Acaa	00 $\Phi_z$ /00 $\Phi_z$	$a^0a^0c^-/a^0a^0c^-$	6.68	4.98	3.98
Acmm	$\Phi\Phi 0$ / $-\Phi-\Phi 0$	$a^-a^-c^0/a^-a^-c^0$	6.83	5.02	4.01
Amam	$\Phi\Phi 0$ / $\Phi\Phi 0$	$a^-a^-c^0/a^-a^-c^0$	6.26	4.81	3.80
Amam	$\Phi\Phi\text{dis}$ / $\Phi\Phi\text{dis}$	$a^-a^-c^{\text{dis}}/a^-a^-c^{\text{dis}}$	6.19	4.78	3.77
A2 <sub>1</sub> am	$\Phi\Phi\Psi_z$ / $\Phi\Phi\Psi_z$	$a^-a^-c^+/a^-a^-c^+$	6.08	4.73	3.72
A2/a	$\Phi\Phi\Phi_z$ / $\Phi\Phi\Phi_z$	$a^-a^-c^-/a^-a^-c^-$	5.75	4.60	3.64

**Table 1:** Fitting statistics from the structural refinement of  $\text{La}_2\text{SrCr}_2\text{O}_7$  using models based on the distortions of  $n = 2$  Ruddlesden-Popper phases.  $\Phi$  indicates an out of phase rotation,  $\Psi$  indicates an in-phase rotation, dis indicates a disordered rotation.

models were constructed to describe  $\text{La}_2\text{SrCr}_2\text{O}_7$  with each of these cooperative distortions, and these models were refined against the neutron powder diffraction data. We have adjusted some of the space group settings from those described by Aleksandrov and Bartolome,<sup>25</sup> as described in the Supporting Information. During the refinement of the models, all atomic positional and displacement parameters were allowed to refine freely, and the La/Sr distribution over the 9-coordinate and 12-coordinate A-cation sites was allowed to refine within the constraints of the total sample composition and that each cation site must remain fully occupied. Close inspection of the neutron diffraction data revealed a set of weak additional diffraction peaks consistent with the presence of small amount of  $\text{LaCrO}_3$ , and so this was added to the model as a second phase.

The refinement of all models proceeded smoothly and it became clear that the two structural models which are distorted by rotating octahedra around all three Cartesian axes (A2<sub>1</sub>am and A2/a) give superior fits to the data compared to models which only rotate the octahedra around one or two of the three Cartesian axes. The symmetry analysis by Aleksandrov and Bartolome shows that in addition to the A2<sub>1</sub>am and A2/a models there is a further '3-twist' cooperative distortion described in space group  $Pnam$  ( $\Phi\Phi\Psi_z$ / $\Phi\Phi-\Psi_z$ ) which should be considered as it can be thought of as a hybrid of the A2<sub>1</sub>am and A2/a distortions. Attempts to refine this model against the data were unsuccessful as strong diffraction features predicted by the model were not observed in the data ( $\chi^2 \sim 8.5$ ). An additional model in which the twisting of the octahedra around the z-axis is disordered (space group *Amam*) was also considered and refined against the data. To support the spacegroup symmetry determination, SHG measurements were performed on  $\text{La}_2\text{SrCr}_2\text{O}_7$ . No SHG signal could be observed, within the sensitivity of the apparatus, strongly suggesting that  $\text{La}_2\text{SrCr}_2\text{O}_7$  adopts a centrosymmetric crystal structure.

The fitting statistics of the 7 different models are given in Table 1. It can clearly be seen that the  $\Phi\Phi\Phi_z$ / $\Phi\Phi\Phi_z$  distortion model in space group A2/a gives the best fit to the data. Further support for the A2/a model comes from examining the refined structure in space group A2<sub>1</sub>am as this model yields chemically unrealistic A-cation arrangements (as described in detail in the supporting information) which in combination with the lack of observed lack of SHG activity, eliminate this model from consideration. We therefore conclude the structure of  $\text{La}_2\text{SrCr}_2\text{O}_7$  is best described by the A2/a model. Details of the refined structure of  $\text{La}_2\text{SrCr}_2\text{O}_7$  are given in Table 2. Selected bond lengths (Table S1) and plots of the observed and calculated data (Figure S1) are shown in the Supporting Information. A representation of the refined structure of  $\text{La}_2\text{SrCr}_2\text{O}_7$  is shown in Figure 1.

**Magnetic Characterization of  $\text{La}_2\text{SrCr}_2\text{O}_7$ .** Magnetization data collected from  $\text{La}_2\text{SrCr}_2\text{O}_7$  in an applied field of 100 Oe show a divergence between zero-field cooled and field cooled data below 285K which increases dramatically below 260K with an associated local maximum in the zero-field cooled data at this temperature,

Atom	x	y	z	Fraction	$U_{\text{iso}}$ ( $\text{\AA}^2$ )
La/Sr(1)	1/4	0.7416(9)	0	82(2)/17(2)	0.0069(1)
La/Sr(2)	0.2449(8)	0.7485(6)	0.1818(1)	58(1)/42(1)	0.0056(2)
Cr(1)	0.2509(16)	0.2491(14)	0.0974(1)	1	0.0013(1)
O(1)	1/4	0.2205(12)	0	1	0.0096(3)
O(2)	0.9869(10)	0.9981(25)	0.1008(1)	1	0.0098(1)
O(3)	0.5055(9)	0.5025(21)	0.0921(1)	1	0.0106(2)
O(4)	0.2412(13)	0.2649(8)	0.1982(1)	1	0.0091(3)

$\text{La}_2\text{SrCr}_2\text{O}_7$  – space group: A2/a

$a = 5.4917(3)$   $\text{\AA}$ ,  $b = 5.4798(3)$   $\text{\AA}$ ,  $c = 20.181(1)$   $\text{\AA}$ ,  $\beta = 89.87(1)^\circ$   
volume =  $607.35(9)$   $\text{\AA}^3$

phase fraction = 96.7(1) weight percent

$\text{LaCrO}_3$  – space group: Pnma

$a = 5.469(2)$   $\text{\AA}$ ,  $b = 7.762(5)$   $\text{\AA}$ ,  $c = 5.512(2)$   $\text{\AA}$

phase fraction = 3.3(1) weight percent

$\chi^2 = 5.75$ , wRp = 4.60%, Rp = 3.64%

**Table 2:** Structural parameters for  $\text{La}_2\text{SrCr}_2\text{O}_7$  refined against neutron powder diffraction data collected at 298K.

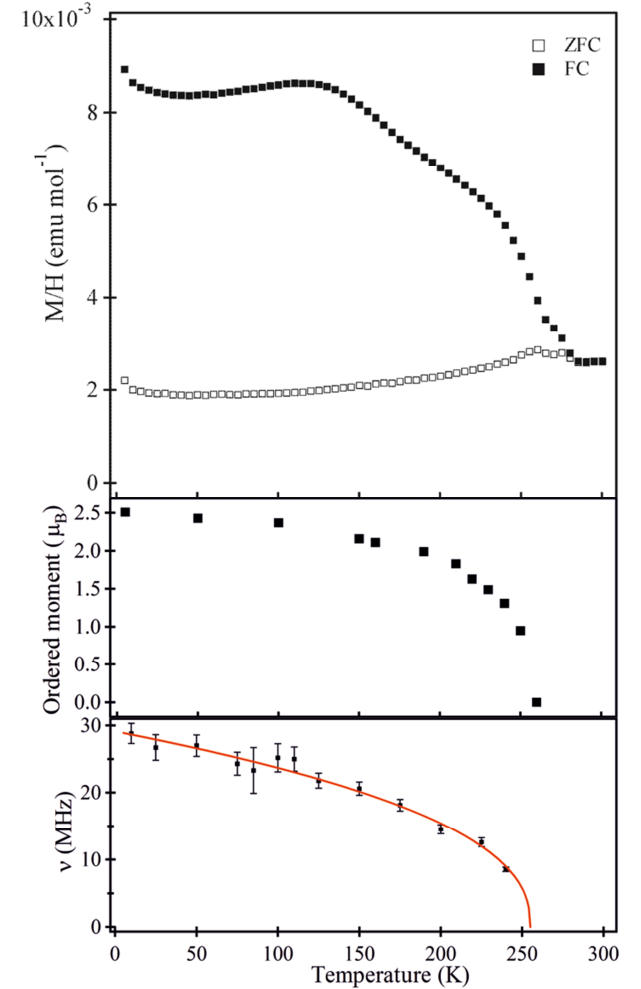


**Figure 2.** Plots of zero-field cooled and field cooled magnetization (top), ordered magnetic moment extracted from fits to neutron powder diffraction data (middle) and muon oscillation frequency (bottom) collected as a function of temperature from  $\text{La}_2\text{SrCr}_2\text{O}_7$ .

consistent with canted antiferromagnetic behavior, as shown in Figure 2.

Neutron powder diffraction data collected from  $\text{La}_2\text{SrCr}_2\text{O}_7$  at 5 K show additional diffraction features compared to analogous data collected at 298K, consistent with the presence of magnetic order at low temperature. The additional diffraction features can be indexed using the crystallographic unit cell indicating a magnetic ordering vector  $\mathbf{k} = 0$ . A magnetic symmetry analysis using the Sarah code<sup>26</sup> was performed on  $\text{La}_2\text{SrCr}_2\text{O}_7$  (space group  $A2/a$ ) to yield 4 irreducible representations each consisting of 3 basis vectors, as described in the supporting information. These symmetry compatible magnetic models were refined against the low-temperature neutron diffraction data and it was observed that the magnetic diffraction intensity was best accounted for using the irreducible representation corresponding to Shubnikov group  $A2''a'$  which is a G-type antiferromagnetic model with spins aligned parallel to the crystallographic  $b$ -axis as shown in Figure 3. This irreducible representation allows for weak ferromagnetism along both the crystallographic  $a$ - and  $c$ -axes (consistent with the weak ferromagnetism observed in the magnetization data) however these components of the magnetic lattice were too small to extract from the diffraction data, so were set to zero.

Neutron powder diffraction data collected on warming the sample indicate that the ordered moment of  $\text{La}_2\text{SrCr}_2\text{O}_7$  declines from a value of  $2.51(3) \mu_B$  per chromium center at 5K to zero at 260 K, as shown in Figure 2. Strong persistent oscillations were observed in zero-field  $\mu^{\text{SR}}$  data collected from  $\text{La}_2\text{SrCr}_2\text{O}_7$  at 5 K, consistent with long range antiferromagnetic order (Figure S4). These oscillations declined in frequency with increasing temperature and ultimately disappeared from the signal at  $T \sim 260$  K, as shown in Figure 2, in agreement with the antiferromagnetic ordering temperatures observed in the magnetization and neutron diffraction data.

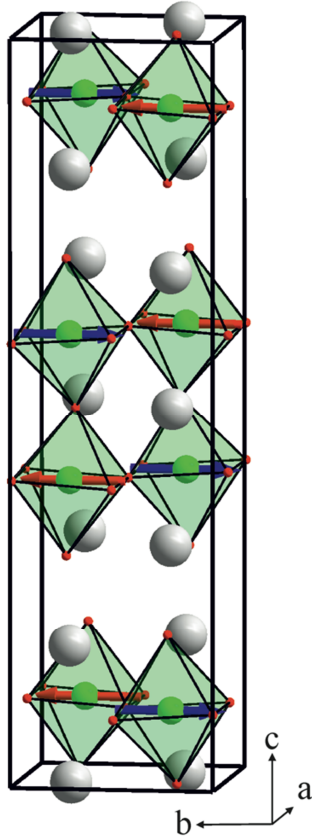


**Figure 3.** The magnetic structure of  $\text{La}_2\text{SrCr}_2\text{O}_7$  refined from neutron diffraction data at 5K. Ordered moment =  $2.51(3) \mu_B$  per Cr center.

## Discussion

While it is clear from diffraction data that  $\text{La}_2\text{SrCr}_2\text{O}_7$  crystallizes with an  $n = 2$  Ruddlesden-Popper type structure, deducing which of the many cooperatively distorted structures it adopts is more challenging. The structural distortions differ from the high-symmetry, aristotype  $n = 2$  Ruddlesden-Popper structure by small displacements of the oxide ions and A-cations and so leave only modest signatures in the diffraction data. As a result it is necessary to use a variety of symmetry-based arguments to confirm that the  $\Phi\Phi\Phi_z / \Phi\Phi\Phi_z$  distortion model in space group  $A2/a$ , which refines to give the best statistical fit to the diffraction data, is actually the distorted structure adopted.

Of the three distorted  $n = 2$  Ruddlesden-Popper structures that refine to give the best statistical fits to the diffraction data ( $Amam$ ,  $A2_1am$ ,  $A2/a$ ), the lack of SHG activity eliminates the polar  $A2_1am$  structure from consideration. In addition, the observation of weak ferromagnetism in combination with G-type antiferromagnetic order is incompatible with the distorted structures in space group  $Amam$  (ordered or disordered). Thus the  $A2/a$  distorted model is the only remaining candidate structure. The validity of the structural assignment is further reinforced by the observation that only the  $A2/a$  model yields a structure with chemically realistic atom displacements.

To the best of our knowledge, this is the first report of an  $n = 2$  Ruddlesden-Popper phase adopting a  $\Phi\Phi\Phi_z / \Phi\Phi\Phi_z$  distorted structure. Given that the major driving force for the distortion of  $\text{A}_3\text{B}_2\text{O}_7$ ,  $n = 2$  Ruddlesden-Popper phases is thought to be the mismatch in A- and B-cation radii, it is rather unexpected that  $\text{La}_2\text{SrCr}_2\text{O}_7$  adopts a novel structural distortion because the ratio of A- to B-cation radii, as measured by  $t$ , the tolerance factor, is similar to that of many other  $n = 2$  Ruddlesden-Popper phases, which adopt more common structural distortions. For example, using Shannon ionic radii to estimate the tolerance factor of phases,<sup>27</sup> we observe that the value calculated for  $\text{La}_2\text{SrCr}_2\text{O}_7$  ( $t = 0.977$ ) lies between those of  $\text{La}_2\text{SrFe}_2\text{O}_7$  ( $t = 0.963$ ) and  $\text{La}_2\text{BaFe}_2\text{O}_7$  ( $t = 0.983$ ) both of which crystallize with undistorted structures (space group  $I4/mmm$ ),<sup>28</sup> leading to the expectation that  $\text{La}_2\text{SrCr}_2\text{O}_7$  would do likewise.

An explanation of the unusual distorted structure adopted by  $\text{La}_2\text{SrCr}_2\text{O}_7$  can be provided by observing that in addition to the unusual tilting scheme, the phase also exhibits a highly unusual distribution of the La and Sr cations over the 9-coordinate ‘rocksalt’ and 12-coordinate ‘perovskite’ A-sites of the lattice. A survey of  $n = 2$  Ruddlesden-Popper phases which have two or more different A-cations reveals the larger cation will preferentially occupy the 12-coordinate perovskite A-site, with the degree of ‘A-cation order’ exhibited by a phase (i.e. the degree of deviation from a purely statistical cation distribution) being dependent on the difference in size and/or charge between the different A-cations. Thus for example  $\text{YSr}_2\text{Mn}_2\text{O}_7$  and  $\text{HoSr}_2\text{Mn}_2\text{O}_7$ <sup>29</sup> adopt structures with as strong preference for locating the larger  $\text{Sr}^{2+}$  cation on the 12-coordinate A-site due to the large difference in the radii of  $\text{Y}^{3+}/\text{Ho}^{3+}$  compared to  $\text{Sr}^{2+}$  (9CN radius:  $\text{Y}^{3+} = 1.075 \text{ \AA}$ ;  $\text{Ho}^{3+} = 1.072 \text{ \AA}$ ;  $\text{Sr}^{2+} = 1.31 \text{ \AA}$ ).<sup>27</sup> In contrast  $\text{LaSr}_2\text{Mn}_2\text{O}_7$  and  $\text{NdSr}_2\text{Mn}_2\text{O}_7$  adopt structures with statistical A-cation disorder<sup>30,31</sup> due to the small size difference between  $\text{La}^{3+}/\text{Nd}^{3+}$  and  $\text{Sr}^{2+}$  (9CN radius:  $\text{La}^{3+} = 1.21 \text{ \AA}$ ;  $\text{Nd}^{3+} = 1.16 \text{ \AA}$ ).<sup>27</sup> In this case A-cation order can be recovered by reestablishing the size difference between  $\text{Ln}^{3+}$  and  $\text{AE}^{2+}$ , by replacing  $\text{Sr}^{2+}$  with  $\text{Ba}^{2+}$  (9CN radius:  $\text{Ba}^{2+} = 1.57 \text{ \AA}$ ),<sup>27</sup> as observed for  $\text{Nd}_2\text{BaMn}_2\text{O}_7$ <sup>32</sup>.

The structural trends described above lead us to expect that the  $\text{La}^{3+}$  and  $\text{Sr}^{2+}$  cations present in  $\text{La}_2\text{SrCr}_2\text{O}_7$  will distribute themselves over the A-cation sites in the  $n = 2$  Ruddlesden-Popper lattice to favor the location of  $\text{Sr}^{2+}$  on the 12-coordinate perovskite A-site, or at a minimum to have a statistical 66:33 La:Sr cation distribution on both the 9- and 12-coordinate A-sites. However, as shown in Table 2, the perovskite A-sites of  $\text{La}_2\text{SrCr}_2\text{O}_7$  are occupied by 82(2)%  $\text{La}^{3+}$  and 18(2)%  $\text{Sr}^{2+}$ , while the rocksalt A-sites are occupied by 58(1)% La and 42(1)% Sr – the reverse of what is expected. As a result the average radius of the cations on the perovskite A-site is

smaller than those on the rocksalt A-site, suggesting this highly unusual situation could be the origin of the usual structural distortion observed for  $\text{La}_2\text{SrCr}_2\text{O}_7$ .

**First-Principles Theory.** We performed a series of first-principles Density Functional Theory calculations in order to gain further insight into the unexpected A-site cation ordering pattern and  $\Phi\Phi\Phi_z/\Phi\Phi\Phi_z$  tilting scheme observed for  $\text{La}_2\text{SrCr}_2\text{O}_7$ . Are these two structural features related, and if so, how? As we are focused on structural features and trends we assumed ferromagnetic ordering of spins on the Cr ions throughout most of our analysis. We verified that antiferromagnetic ordering of spins does not qualitatively change our results, as explained in the Supporting Information.

First, we performed full structural relaxations starting from the experimentally determined structural coordinates for the space groups and tilting schemes shown in Table 1; the Sr and La cations were placed on their expected sites, that is, Sr on the 12-coordinate perovskite A-site and La on the 9-coordinate rocksalt A-site. The  $Acaa$  and  $Acmm$  structures both relaxed into  $I4/mmm$ , whereas the  $A2/a$ ,  $A2_1am$  and  $Pnam$  structures relaxed into  $Amam$ . In other words, tilts about the  $c$  axis relaxed out for each structure, suggesting that octahedral tilts about  $c$  are energetically unfavorable without some disordering of the Sr and La sites. This is further corroborated by phonon calculations on  $\text{La}_2\text{SrCr}_2\text{O}_7$  in the  $I4/mmm$  and  $Amam$  space groups: lattice modes corresponding to octahedral tilts about  $c$  are stable (have real frequencies) in both space groups, indicating that such distortions are not energetically favorable.

Next, we explored the effects of Sr/La disorder by starting from a fully relaxed  $I4/mmm$  structure and systematically generating a series of symmetry-unique structures (for a 24-atom simulation cell) with differing Sr/La distributions. Within this unit cell, any A-site disorder breaks the  $I4/mmm$  symmetry with the resulting space group depending on the exact distribution of Sr and La cations. We found that without any structural relaxation, switching any Sr cation in a 12-coordinate site with any La-cation in a 9-coordinate site raises the energy by at least 0.8 eV/formula unit (f.u.).

After full structural relaxation, the  $I4/mmm$  structure with Sr and La on their expected sites remains the lowest in energy by approximately 20 meV/f.u. Hence, our results thus far suggest that without some disordering of the Sr/La sites, octahedral tilts about the  $c$  axis are energetically unfavorable, but without octahedral tilts the Sr and La cations prefer to be in the perovskite and rocksalt layers respectively. Disordering of the Sr and La cations appears to be related to the experimental observation of the  $\Phi\Phi\Phi_z/\Phi\Phi\Phi_z$  tilting scheme – why?

Our computational framework does not allow for fractional occupancies, so it was necessary to investigate structures with many different specific distributions of Sr/La in order to enable comparisons between theory and experiment. Rather than trying to exactly reproduce the observed Sr/La distribution, our goal was rather to explore structural trends across a range of different distributions, which includes the experimentally observed one. Starting from a 48-atom simulation cell (four formula units), we constructed a series of structures with the following Sr/La distributions: 0/100 in rock salt, 100/0 in perovskite; 12.5/87.5 in rock salt, 75/25 in perovskite; 25/75 in rock salt, 50/50 in perovskite; 37.5/62.5 in rock salt, 25/75 in perovskite; 50/50 in rock salt, 0/100 in perovskite. Hence, this simulation cell can accommodate Sr/La distributions that approximate the observed one (42/58 in rock salt, 18/82 in perovskite) reasonably closely as well as the various octahedral twisting patterns considered in the experimental structure refinements. Investigating every possible arrangement of Sr and La cations for each distribution would be extremely computationally intensive (there are approximately 500 possible – not necessarily symmetry unique – structures for the 48-atom unit cell we are using), so we selected 36 arrangements “by hand” with a mix of the Sr/La distributions listed above. We noticed from our calculations in a 24-atom simulation cell that structures with multiple adjacent Sr cations tended to have higher energies. This

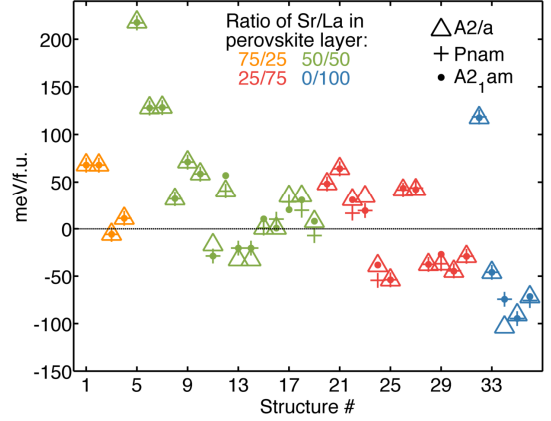


**Figure 4.** Relaxed energies per formula unit (f.u.) of our 108 structures with varying La/Sr distributions with respect to the energy of the  $Amam$  reference structure with La/Sr cations on their expected sites (we take the energy of this structure to be the zero of energy, indicated by the horizontal dashed line). Color and shape of points indicate the ratio of Sr/La distribution and initial ionic positions respectively. Note that in many cases plot symbols overlap. The horizontal axis is labeled by arbitrary structure numbers corresponding to Table S3. The structures are sorted by the Sr/La ratio and the mean distance between Sr cations in our relaxed  $Amam$  structure after swapping Sr/La positions, but before any further relaxation. A general tendency for energy to be lowered as the Sr cations spread out is evident.

tendency prompted us to select arrangements with the Sr cations spread out in a 48-atom simulation cell, which we expected to also be lower in energy. We also included several arrangements with clusters of Sr cations that we expected to be high in energy for comparison. For each arrangement of Sr/La, we performed a relaxation starting from the experimental coordinates for  $\text{La}_2\text{SrCr}_2\text{O}_7$  in  $A2/a$ ,  $Pnam$  and  $A2_1am$ ; this produced  $36 \times 3 = 108$  structures with varying Sr/La distributions for further investigation. We expect this set of structures is sufficient to study structural and energetic trends relevant to the experimental data. The full list of structures we considered and the symmetry of each is enumerated in Table S3 in the Supporting Information. Note that due to the A-site cation disorder, our final, relaxed structures are lower in symmetry than the starting  $A2/a$ ,  $Pnam$  and  $A2_1am$  structures.

Each of the  $A2/a$ ,  $Pnam$  and  $A2_1am$  space groups is a subgroup of  $Amam$  (with the La and Sr ions in their expected positions) and differ in the pattern of octahedral tilting about the  $c$  axis. We thus use  $Amam$  as a reference structure, since  $\text{La}_2\text{SrCr}_2\text{O}_7$  in this space group does not have octahedral tilts about  $c$ . Figure 4 shows that various distributions of Sr/La can result in structures that are lower in energy than the  $Amam$  reference structure with Sr and La on their expected sites. The relaxations starting from  $A2/a$ ,  $Pnam$  and  $A2_1am$  always resulted in three structures with similar energies. The three initial structures relaxed into identical structures for some of the Sr/La distributions, but in these cases the relaxed energy is typically higher than that of the  $Amam$  reference structure. The energies shown in Figure 4 are shown again in Figure S6, in the Supporting Information, with the  $x$ -axis changed to be the mean Sr-Sr distance, confirming the general trend that A-site arrangements with Sr cations spread out are lower in energy.

Thorough examination of the low energy (compared to  $Amam$ ) relaxed structures in Figure 4 revealed that the lowest energy structure for each Sr/La distribution has  $A2/a$ -like octahedral tilts about  $c$ , with a single exception. Sometimes one or both of the relaxations started from  $Pnam$  or  $A2_1am$  coordinates relaxed into the same structure as the relaxation started from  $A2/a$  coordinates. For the low energy

Sr/La distributions, these identical structures have octahedral tilts about  $c$  corresponding to the  $A2/a$  symmetry. Since the lowest energy structure for all but one of the Sr/La distributions has primarily  $A2/a$ -like octahedral tilts about  $c$ , we conclude it is the most stable space group and now focus on analyzing structural trends within the  $A2/a$ -like structures.

We analyzed structural trends among the 36  $A2/a$ -like structures to better understand the interplay between A-site disorder and octahedral tilts. The large number of structures, combined with their low symmetry and Sr/La disorder, demanded a systematic, quantitative approach. We decided to focus on searching for correlations between octahedral tilts about  $c$  (since the experimentally considered structures differ in their  $c$ -axis tilting patterns) and other structural features. The first challenge was to determine how to quantify the magnitude of tilting about the  $c$  axis. We would normally perform a rigorous symmetry-adapted mode analysis to obtain such information, but in this case A-site disorder makes such an approach extremely challenging. As an alternative we used bond valence discrepancy factors to quantify the average bonding environment of the equatorial oxygen atoms  $O_{eq}$  (that is, the oxygen atoms that reside in the  $CrO_2$  layers) which will be directly affected by octahedral tilts about  $c$ . The discrepancy factor<sup>33</sup> is defined as the difference between the formal valence of a particular ion, and the calculated bond valence sum for the same ion in the structure of interest. A discrepancy factor of zero thus indicates that the ion is ideally coordinated. A positive discrepancy factor indicates underbonding (the cation-anion bonds are too long compared to the ideal, strain-free coordination environment in the bond valence model), whereas a negative discrepancy factor indicates overbonding (cation-anion bonds are too short). In addition, we calculated the values of 47 different structural features for each of our relaxed materials and performed a linear correlation analysis to guide the search for trends between these features and the bonding environment of the equatorial oxygens. The structural features included, for example, Cr-O-Cr bond angles,  $CrO_6$  volumes and distortion indices (defined as the average fractional deviation of Cr-O bond lengths from the average Cr-O bond length in a  $CrO_6$  octahedron<sup>34</sup>), and bond valence discrepancy factors for each atom; the full list of features, along with details of our linear correlation analysis, can be found in the Supporting Information. Our analysis revealed strong correlations between the bonding environment of the  $O_{eq}$  anions and the average maximum Cr-O bond length, the Cr-O-Cr “in-plane” angle (this is the Cr-O-Cr angle assuming the three ions lie in the same plane, which emphasizes octahedral rotations about  $c$  rather than the in plane axes that dominate the Cr-O-Cr), the ratio of Sr to La in the perovskite layer, the average  $CrO_6$  distortion index and the average discrepancy factor of La cations in the rock salt layers ( $La_{rs}$ ). We take averages for certain quantities because there is more than one unique atomic environment for the atoms of interest. What do these correlations mean chemically and physically?

Figure 5 shows a plot of the average  $CrO_6$  distortion index against the discrepancy factors of both the  $O_{eq}$  anions, and the  $La_{rs}$  cations, for  $A2/a$  energy minimized structures with a range of Sr/La cation distributions. The analogous discrepancy factors from the Sr/La cation-ordered  $Amam$  reference structure are also plotted in Figure 5. If we first consider the broad relationship between the Sr/La distribution (as indicated by the color of the points in Figure 5) and the  $CrO_6$  distortion index, we observe that the  $CrO_6$  distortion index in the  $Amam$  reference structure (0.02578) is much larger than typically observed experimentally in other  $Cr^{3+}$  oxides. For comparison the distortion indices of  $Cr^{3+}O_6$  octahedra in the experimentally determined structures for  $BiCrO_3$ ,  $LaCrO_3$ ,  $PrCrO_3$ ,  $GdCrO_3$ ,  $TbCrO_3$ ,  $YCrO_3$ ,  $HoCrO_3$ ,  $TmCrO_3$ ,  $YbCrO_3$ ,  $LuCrO_3$ ,  $InCrO_3$  and  $ScCrO_3$  are respectively 0.00268,<sup>35</sup> 0.01143,<sup>36</sup> 0.00488,<sup>36</sup> 0.00181,<sup>36</sup> 0.0423,<sup>36</sup> 0.0044,<sup>36</sup> 0.00347,<sup>36</sup> 0.00083,<sup>36</sup> 0.00455,<sup>36</sup> 0.00445,<sup>36</sup> 0.01032,<sup>37</sup> and 0.00651.<sup>37</sup> The remaining data in Figure 5 show that as an increasing fraction of the Sr cations are moved into the rock salt layer, the  $CrO_6$  distortion index decreases dramatically. Further insight into this

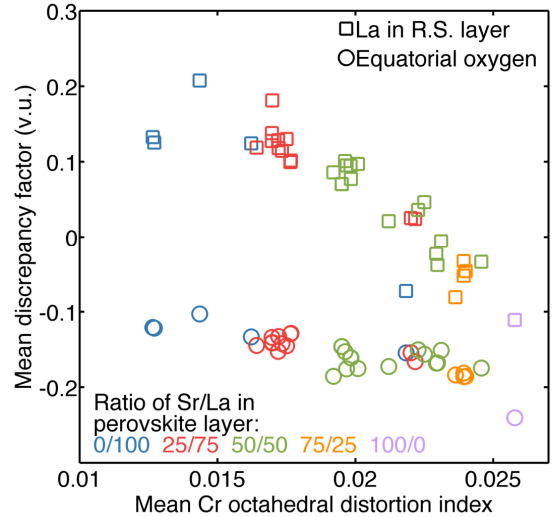


**Figure 5.** The average discrepancy factor, in valence units (v.u.) of La cations in the rock salt layer and equatorial oxygen ions as a function of the average  $CrO_6$  distortion index with various A-site distributions. Light purple points correspond to the reference  $Amam$  structure with the expected A-site cation ordering.

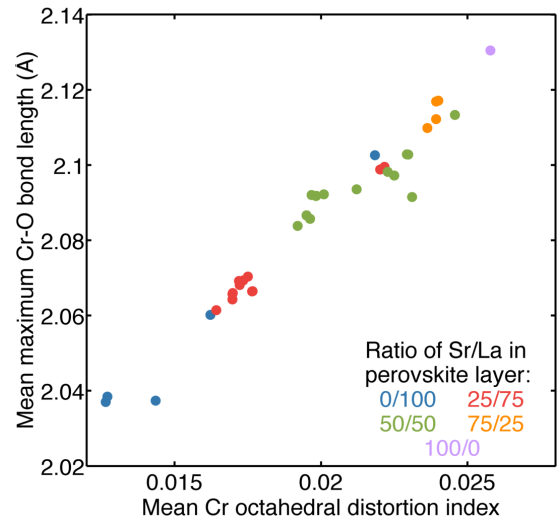


**Figure 6.** The average maximum Cr-O bond length as a function of the average  $CrO_6$  distortion index with various A-site distributions. Light purple points correspond to the reference  $Amam$  structure with the expected A-site cation ordering. As the mean maximum Cr-O bond length increases, the mean  $CrO_6$  distortion index increases linearly. The maximum of each is reached in the  $Amam$  structure with La and Sr cations on their expected sites.

observation can be gained by noting that there is an almost linear relation between the average maximum Cr-O bond length and  $CrO_6$  distortion index, as shown in Figure 6. This highlights the fact that the relatively large  $CrO_6$  distortion index observed for the cation-ordered  $Amam$  reference structure can be attributed to a single long bond between the chromium and the axial oxide ion residing within the rock salt layer. As more strontium is moved into the rock salt layers, this axial Cr-O bond length decreases, and thus the  $CrO_6$  distortion index decreases.

The coupling between the Sr/La distribution and the Cr-O axial bond length can be accounted for by a simple electrostatic interac-

tion. When the La and Sr cations are ordered within the *Amam* reference structure, there are negatively charged  $\text{CrO}_2$  layers sandwiched between a positively charged  $\text{LaO}$  rock salt layer and a charge neutral  $\text{SrO}$  perovskite layer. In this situation the positively charged Cr atoms displace towards the neutral  $\text{SrO}$  layer, leading to a single long bond between Cr and an apical oxygen in the  $\text{LaO}$  layer. As the La/Sr distribution is disordered, the charges of the rock salt and perovskite AO layers become more even and the tendency for Cr to undergo this distortion decreases, leading to a more uniform set of Cr-O bond lengths. We can therefore see that one of the drivers for the disordering of the La and Sr cations is to decrease the asymmetry of the  $\text{CrO}_6$  units and thus strengthen the Cr-O bonding. However, as noted above, in the absence of octahedral tilts around the *c*-axis, Sr/La disorder is energetically unfavorable, so the strengthening of the Cr-O bonds alone is not sufficient to disorder the A-cations.

An indication of the role of the octahedral rotations in stabilizing the observed structure of  $\text{La}_2\text{SrCr}_2\text{O}_7$  can also be seen in Figure 5, which shows that in addition to the adoption of more symmetric  $\text{CrO}_6$  units, the disordering of the Sr/La cations leads to an improvement in the  $\text{O}_{\text{eq}}$  bonding environment; these oxygen ions are significantly overbonded (compressed) in the Sr/La ordered *Amam* structure, and this overbonding is relieved somewhat by the unusual experimentally observed Sr/La distribution. However, the improvements in the bonding environments of  $\text{O}_{\text{eq}}$  and Cr come at the expense of a deterioration in the  $\text{La}_{\text{rs}}$  bonding environment. The La cations are slightly overbonded in the cation-ordered *Amam* reference structure and become increasingly underbonded as the concentration of Sr in the perovskite layers decreases. How do these observations relate to octahedral tilts about *c*?

Figure 7 shows the same data as Figure 5, but with the average “in-plane” Cr-O-Cr angle as abscissa. Now we see that this angle also decreases from  $180^\circ$  (indicating an increasing magnitude of tilts about *c*) as the concentration of Sr in the perovskite layers decreases, with an associated improvement/deterioration of the  $\text{O}_{\text{eq}}/\text{La}_{\text{rs}}$  bonding environments. Summarizing the arguments above, we observe that the principal driver for the disordering of the La and Sr cations is the desire to lower the charge difference between the La-O rock salt and Sr-O perovskite layers, and thus make the  $\text{CrO}_6$  units more symmetric. As noted previously, in the absence of octahedral tilts around the *c*-axis, the stabilization of the Cr-O bonding is not sufficient to overcome the inherent stability of Sr/La A-site ordered configuration, so Sr/La disorder is not observed. However, in addition to equalizing the charges of the rock salt and perovskite layers, Sr/La disorder locally breaks symmetry about the equatorial oxygens, allowing them to displace and the  $\text{CrO}_6$  units rotate. This allows the  $\text{O}_{\text{eq}}$  bonding to be optimized and in combination the improvement to the bonding of both the chromium and equatorial oxide ions is sufficient to make the cation-disordered,  $\Phi\Phi\Phi_z/\Phi\Phi\Phi_z$  distorted structure more stable than the cation-ordered *Amam* arrangement.

The importance of the optimization of the  $\text{CrO}_6$  bonding as a driving force for the Sr/La cation disorder, and the associated  $\Phi\Phi\Phi_z/\Phi\Phi\Phi_z$  distortion, is highlighted by comparing the  $\text{La}_2\text{SrCr}_2\text{O}_7$  system to other  $n = 2$  Ruddlesden-Popper phases, most notably the  $\text{Fe}^{3+}$  containing  $\text{Ln}_2\text{AEFe}_2\text{O}_7$  (AE = Sr, Ba) series. As noted above  $\text{La}_2\text{SrFe}_2\text{O}_7$  adopts an undistorted  $n = 2$  Ruddlesden-Popper structure (space group  $I4/mmm$ ) with a 53:47 Sr:La ratio on the perovskite A-site.<sup>28</sup> Likewise  $\text{La}_2\text{BaFe}_2\text{O}_7$  adopts an undistorted structure with a 73:37 Ba:La ratio on the perovskite A-site.<sup>28</sup> Thus both phases favour locating the large  $\text{AE}^{2+}$  cation on the perovskite A-site (compared to the 33:66  $\text{AE}^{2+}:\text{La}^{3+}$  ratio expected statistically) and neither exhibit any collective rotations of their  $\text{FeO}_6$  octahedra, in strong contrast to  $\text{La}_2\text{SrCr}_2\text{O}_7$ . A further contrast to the chromium system is that both  $\text{La}_2\text{SrFe}_2\text{O}_7$  and  $\text{La}_2\text{BaFe}_2\text{O}_7$  exhibit highly distorted  $\text{FeO}_6$  units. As noted above the primary distortion mode of the  $\text{CrO}_6$  octahedra in our calculations is the lengthening of the bond between chromium and the axial oxide ion in the rock salt layer. If we define a further distortion parameter,  $\text{MO}_6$ -axial-distort ( $\text{MO}_{6\text{-ad}}$ ), as the ratio of the M-O

bonds to the axial oxide ions in the rock salt and perovskite layers ( $\text{MO}_{6\text{-d}} = \text{M-O}_{\text{rs}}/\text{M-O}_{\text{p}}$ ) then we observe the  $\text{FeO}_6$  units in  $\text{La}_2\text{SrFe}_2\text{O}_7$  and  $\text{La}_2\text{BaFe}_2\text{O}_7$  yield values of 1.12 and 1.14 respectively,<sup>28</sup> compared to a value of 1.03 for  $\text{La}_2\text{SrCr}_2\text{O}_7$ . These observations are

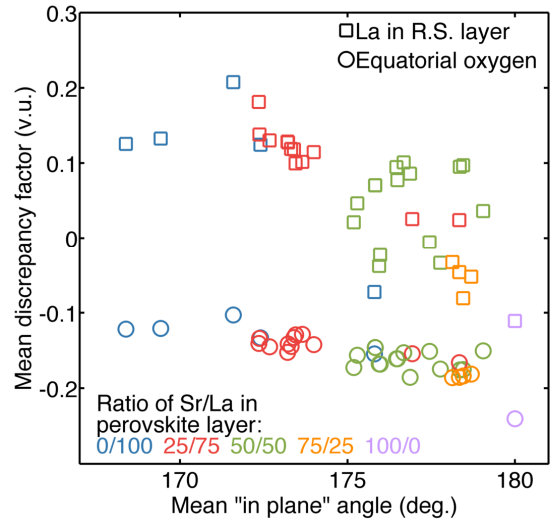


**Figure 7.** The average discrepancy factor of La cations in the rock salt layer and equatorial oxygen ions as a function of the average “in-plane” Cr-O-Cr angle with various A-site distributions. Light purple points correspond to the reference *Amam* structure with the expected A-site cation ordering.

consistent with the idea that i) the ‘normal’ A-cation distribution of  $\text{AE}^{2+}$  on the perovskite A-site and  $\text{La}^{3+}$  on the rock salt A-site induces a distortion into the  $\text{MO}_6$  octahedra and ii) the desire to accommodate the  $\text{Cr}^{3+}$  cations in highly symmetric  $\text{CrO}_6$  units leads to the adoption of the novel A-cation-disordered,  $\Phi\Phi\Phi_z/\Phi\Phi\Phi_z$  distorted structure observed for  $\text{La}_2\text{SrCr}_2\text{O}_7$ .

The strong preference for locating  $\text{Cr}^{3+}$  centers in highly symmetric octahedral coordinations, in comparison to other transition metal cations such as  $\text{Fe}^{3+}$ , is also consistent with similar observations made for  $\text{Cr}^{3+}$  centres in a wide variety of other chemical systems. This wider observation is justified on the basis of the maximum ligand-field stabilization energy (LFSE) associated with the  $t_{2g}^3e_g^0$  local electronic configuration of  $\text{Cr}^{3+}$ , compared to the zero net LFSE for the  $t_{2g}^3e_g^2$  configuration of  $\text{Fe}^{3+}$ .<sup>38</sup> On lowering the symmetry of the  $\text{MO}_6$  units M-O bonding will be compromised, however in the case of  $\text{Fe}^{3+}$  the associated lowering in energy of the occupied  $e_g$  antibonding orbitals will help to mitigate this, reducing the energy penalty for the distortion of  $\text{Fe}^{3+}\text{O}_6$  units compared to  $\text{Cr}^{3+}\text{O}_6$  units. This leads us to suggest that we would expect to see a similar coupling of the A-site cation order and octahedral rotations as observed in  $\text{La}_2\text{SrCr}_2\text{O}_7$  in other  $n = 2$  Ruddlesden-Popper phases which contain ‘undistortable’ transition metal cations, such as the as yet unreported phase  $\text{La}_2\text{SrRh}_2\text{O}_7$ , in which the expected low-spin  $t_{2g}^6e_g^0$  electronic configuration of  $\text{Rh}^{3+}$  should strongly resist distortions to the  $\text{RhO}_6$  octahedra.

## Conclusion

The complex coupling between the rotations of the  $\text{CrO}_6$  octahedra and the La/Sr A-site distribution of  $\text{La}_2\text{SrCr}_2\text{O}_7$  clearly demonstrates that the cooperative, symmetry-lowering distortions of  $n = 2$  Ruddlesden-Popper phases are not solely directed by the structural tolerance factor. Instead it appears that the structures adopted by these phases are determined by a number of different parameters in combination. This multiplicity of factors influencing the distorted structures of  $n = 2$  Ruddlesden-Popper phases provides many opportunities to direct the tilting arrangements in layered perovskite phases, to tune

both the magnitude of the B-O-B angles and the symmetry of the cooperatively distorted network.

In the specific case of  $\text{La}_2\text{SrCr}_2\text{O}_7$  we can see that the apparent energy penalty associated with distorting the  $\text{CrO}_6$  octahedra couples together the A-cation distribution and the octahedral rotations. This suggests that if isovalent A-cation substitutions are made to  $\text{La}_2\text{SrCr}_2\text{O}_7$  (e.g.  $\text{Ca}^{2+}$  for  $\text{Sr}^{2+}$  or a smaller lanthanide for  $\text{La}^{3+}$ ) which lead to changes in the distribution of the  $\text{AE}^{2+}$  and  $\text{Ln}^{3+}$  cations between the A-sites in the perovskite and rock salt layers, there will be resulting changes to the cooperative rotations of the  $\text{CrO}_6$  octahedra over and above those expected on the grounds of the changing tolerance factor. Thus this new coupling between A-site distribution and octahedral rotation could provide a route to realizing as-yet unseen structural configurations and facilitate the preparation of phases with desired polar distortions. In addition there is an intriguing possibility that the coupling could be used 'in reverse' to generate novel A-cation ordering schemes in Ruddlesden-Popper phases by utilizing the inflexibility of certain octahedrally coordinated B-cations.

## ASSOCIATED CONTENT

### Supporting Information

Fits to the data and full details of the structural and magnetic refinement at 298K and 5K; Descriptions of the A-cation displacements in the  $\text{A2/a}$  and  $\text{A2/am}$  structural models; Details of the magnetic symmetry analysis of  $\text{LaSr}_2\text{Cr}_2\text{O}_7$ ; Plots of  $\mu^+$  SR data; Full details of the first principals calculations including the linear correlation analysis of structural parameters.

## AUTHOR INFORMATION

### Corresponding Authors

michael.hayward@chem.ox.ac.uk  
nbenedek@cornell.edu

### Author Contributions

The manuscript was written through contributions of all authors.

## ACKNOWLEDGMENT

We thank W. Kockelmann and I. da Silva for assistance collecting the neutron powder diffraction data. Experiments at the ISIS pulsed neutron facility were supported by a beam time allocation from the Science and Technology Facilities Council. Part of this work was carried out at the Swiss muon source  $\text{S}\mu\text{S}$ , Paul Scherrer Institut, Villigen, Switzerland. The first-principles calculations were carried out using the resources of the Cornell Center for Advanced Computing. TTT and PSH thank the Welch Foundation (Grant E-1457) and the National Science Foundation (DMR-1503573) for support.

## REFERENCES

- (1) Goldschmidt, V. M. *Naturwissenschaften* **1926**, *14*, 477.
- (2) Torrance, J. B.; Lacrore, P.; Nazzari, A. I.; Ansaldo, E. J.; Niedermayer, C. *Phys. Rev. B* **1992**, *45*, 8209-8212.
- (3) Goodenough, J. B.; Longo, J. M. *Landolt-Börnstein Tabellen*; Springer: Berlin, Heidelberg, New York, 1970.
- (4) Rondinelli, J. M.; Fennie, C. J. *Adv. Mater.* **2012**, *24*, 1961-1968.
- (5) Knapp, M. C.; Woodward, P. M. *J. Solid State Chem.* **2006**, *179*, 1076-1085.
- (6) King, G.; Woodward, P. M. *J. Mater. Chem.* **2010**, *20*, 5785.
- (7) Bousquet, E.; Dawber, M.; Stucki, N.; Lichtensteiger, C.; Hermet, P.; Gariglio, S.; Triscone, J. M.; Ghosez, P. *Nature* **2008**, *452*, 732-734.
- (8) Benedek, N. A.; Rondinelli, J. M.; Djani, H.; Ghosez, P.; Lightfoot, P. *Dalton Trans.* **2015**, *44*, 10543-10558.
- (9) Benedek, N. A.; Fennie, C. J. *Phys. Rev. Lett.* **2011**, *106*.
- (10) Mulder, A. T.; Benedek, N. A.; Rondinelli, J. M.; Fennie, C. J. *Advanced Functional Materials* **2013**, *23*, 4810-4820.
- (11) Benedek, N. A. *Inorg. Chem.* **2014**, *53*, 3769-3777.
- (12) Strayer, M. E.; Gupta, A. S.; Akamatsu, H.; Lei, S.; Benedek, N. A.; Gopalan, V.; Mallouk, T. E. *Advanced Functional Materials* **2016**, *26*, 1930.
- (13) Snedden, A.; Knight, K. S.; Lightfoot, P. *J. Solid State Chem.* **2003**, *173*, 309-313.
- (14) Fennie, C. J.; Rabe, K. M. *Appl. Phys. Lett.* **2006**, *88*.
- (15) Goff, R. J.; Keeble, D.; Thomas, P. A.; Ritter, C.; Morrison, F. D.; Lightfoot, P. *Chem. Mater.* **2009**, *21*, 1296-1302.
- (16) Zhang, R.; Read, G.; Lang, F.; Lancaster, T.; Blundell, S. J.; Hayward, M. A. *Inorg. Chem.* **2016**, *55*, 3169.
- (17) Larson, A. C.; Von Dreele, R. B.; Los Alamos National Laboratory Report LAUR 86-748: 2000.
- (18) Kurtz, S. K.; Perry, T. T. *J. Appl. Phys.* **1968**, *39*, 3798.
- (19) Rieckhof, K. E.; Peticola, W. I. *Science* **1965**, *147*, 610.
- (20) Ok, K. M.; Chi, E. O.; Halasyamani, P. S. *Chem. Soc. Rev.* **2006**, *35*, 710.
- (21) Kresse, G.; Furthmüller, J. *Phys. Rev. B* **1996**, *54*, 11169-11186.
- (22) Kresse, G.; Furthmüller, J. *Computational Materials Science* **1996**, *6*, 15-50.
- (23) Blochl, P. E. *Phys. Rev. B* **1994**, *50*, 17953-17979.
- (24) Kresse, G.; Joubert, D. *Phys. Rev. B* **1999**, *59*, 1758-1775.
- (25) Aleksandrov, K. S.; Bartolome, J. J. *Phys.:Condens. Matter* **1994**, *6*, 8219-8235.
- (26) Wills, A. S. *Physica B* **2000**, *276*, 680-681.
- (27) Shannon, R. D. *Acta Cryst.* **1976**, *A32*, 751.
- (28) Gurusinge, N. N. M.; de la Figuera, J.; Marco, J. F.; Thomas, M. F.; Berry, F. J.; Greaves, C. *Mater. Res. Bull.* **2013**, *48*, 3537-3544.
- (29) Battle, P. D.; Millburn, J. E.; Rosseinsky, M. J.; Spring, L. E.; Vente, J. F. *Chem. Mater.* **1997**, *9*, 3136.
- (30) Battle, P. D.; Green, M. A.; Laskey, N. S.; Millburn, J. E.; Radaelli, P. G.; Rosseinsky, M. J.; Sullivan, S. P.; Vente, J. F. *Phys. Rev. B* **1996**, *54*, 15967-15977.
- (31) Kubota, M.; Oohara, Y.; Yoshizawa, H.; Fujioka, H.; Shimizu, K.; Hirota, K.; Moritomo, Y.; Endoh, Y. *J. Phys. Soc. Jpn.* **2000**, *69*, 1986-1989.
- (32) Meng, J.; Satoh, H.; Ishida, M.; Kamegashira, N. *J. Alloys Compounds* **2006**, *408*, 1182-1186.
- (33) Rao, G. H.; Barner, K.; Brown, I. D. *J. Phys.:Condens. Matter* **1998**, *10*, L757-L763.
- (34) Baur, W. H. *Acta Crystallogr. Sect. B-Struct. Commun.* **1974**, *30*, 1195-1215.
- (35) Darie, C.; Goujon, C.; Bacia, M.; Klein, H.; Toulemonde, P.; Bordet, P.; Suard, E. *Solid State Sci.* **2010**, *12*, 660-664.
- (36) Prado-Gonjal, J.; Schmidt, R.; Romero, J. J.; Avila, D.; Amador, U.; Moran, E. *Inorg. Chem.* **2013**, *52*, 313-320.
- (37) Belik, A. A.; Matsushita, Y.; Tanaka, M.; Takayama-Muromachi, E. *Chem. Mater.* **2012**, *24*, 2197-2203.
- (38) Greenwood, N. N.; Earnshaw, A. *Chemistry of the Elements*; Pergamon Press: Oxford, 1997.

## SYNOPSIS TOC

The  $n = 2$  Ruddlesden-Popper phase  $\text{La}_2\text{SrCr}_2\text{O}_7$  adopts a highly unusual structural configuration in which the cooperative rotations of the  $\text{CrO}_6$  octahedra are out of phase in all three Cartesian directions ( $\Phi\Phi\Phi_z/\Phi\Phi\Phi_z; a^-a^-c^-/a^-a^-c^-$ ). First principles DFT calculations indicate that this unusual structural arrangement can be attributed to coupling between the La/Sr A-site distribution and the rotations of the  $\text{CrO}_6$  units, which combine to relieve the local deformations of the chromium-oxygen octahedra.

